Bayesian Inference for Updating Chatter Model Parameters in Turning

Keivan Ahmadi[a,*]

[a]*Department of Mechanical Engineering, University of Victoria, Victoria, British Columbia, Canada V8W 2Y2.*

Abstract

Variations in the mechanics and dynamics of the machining process under operational conditions cause inaccuracies in chatter model predictions. The parameters of chatter models therefore require re-calibration based on experimental observations during the process.

Focusing on turning operations, this paper takes a Bayesian model updating approach to present a new method for in-process calibration of chatter model parameters. The presented new method identifies the dominant closed-loop pole of the machining system from in-process vibrations and updates the probability distribution of the model parameters based on the identified poles. Compared to existing methods, which require experimental observations under both stable and unstable conditions, the presented method requires a limited set of vibration measurements during stable conditions only. Moreover, the updated probability distributions are used to establish credibility bounds around the Stability Lobe Diagrams (SLD). An experimental example is presented to demonstrate the efficiency and effectiveness of the presented method in enhancing the accuracy of chatter predictions in turning.

1. Introduction

Instability of process-induced vibrations during machining, known as regenerative chatter, can damage the machine tool or the finished surface. Mod-

*Corresponding author

eling and control of chatter in various machining operations is a well-studied topic, and chatter models are now being used by the industry to design high-performance operations [1]. Nonetheless, existing models usually show some degree of inaccuracy in predicting chatter, mainly due to the uncertainty of their parameters. For instance, the machine tool's modal parameters are usually determined by modal testing when the machine is idle but vary significantly under operational conditions. Since those parameters are critical in chatter models, their variations cause a significant inaccuracy in chatter predictions. Similarly, tool wear during the process can change the parameters of the cutting force models, directly influencing the accuracy of chatter predictions. To continuously improve the accuracy of chatter predictions during the process, model parameters must therefore be updated based on the experimental data collected during machining.

In-process identification of model parameters can reduce their uncertainty and improve the accuracy of chatter models. Minis et al. [2] identified the tool-tip Frequency Response Functions (FRF) used in chatter models based on the force and vibration signals measured during a turning process. Because the frequency content of machining forces are not rich enough to excite the normal modes of the machine tool, a specialized workpiece with pseudo random surface pattern was designed in [2] to enrich the frequency spectrum of machining forces. A similar approach was adopted by Ozsahin et al. [3] to identify the tool-tip FRF in milling. Zaghbani and Sogmene [4] used Operational Modal Analysis (OMA) to identify the modal frequency and damping values in a milling system from the vibration signals measured during the process. In-process calibration of force model parameters can also improve the accuracy of chatter models. For instance, Farhadmanesh and Ahmadi [5] presented online identification methods for calibrating the specific force coefficients in mechanistic force models. Using this method, force model parameters can be calibrated adaptively as tool wear increases or cutting conditions change. In-process model parameter identification requires using force sensors (e.g. dynamometers), which usually have a limited bandwidth and are cumbersome to

use in production. Operational Modal Analysis does not need force sensors, but it cannot identify mass-normalized mode shapes that are necessary for chatter modeling. Besides, in-process modal parameter identification requires designing specialized processes, because machining forces in regular operations are usually not persistently exciting for identifying machine tool dynamics.

Chatter model parameters can also be calibrated based on the stability of vibrations observed during the process. A systematic method with this approach was presented by Ozsahin et al. [6], where the depth of cut above which vibrations become unstable at a given spindle speed is determined experimentally and used in the theoretical chatter model to calibrate its parameters. This inverse stability analysis approach was further improved by Grossi et al. [7], Eynian [8], and Liu and Altintas [9]. The calibration accuracy in this method hinges on the accuracy of experimentally identified chatter limits. Detecting vibration instability, especially close to stability borders, is sometimes difficult and inaccurate, because there may not be a clear transition from stable to unstable vibrations. Moreover, inverse stability analysis requires conducting multiple experiments under chatter conditions which is not practical in industrial applications.

With the widespread use of data-driven (machine learning) methods in various fields, those methods have found great applications in improving the accuracy of chatter models in machining as well. Postel et al. [10] combined a physics-based chatter model with an Artificial Neural Network (ANN) in series such that some of the parameters of the chatter model are provided by the outputs of the ANN. The overall model parameters were updated by adjusting the weights of the network based on chatter observations during the process. Purely data-driven models are also used to predict chatter [10, 11], and both of these approaches improve the accuracy of the chatter model solely based on observations during regular machining process. Despite this advantage, training the data-driven model requires a great number of chatter encounters during the process, which undermines its applicability in production environment.

In this paper, focusing on turning operations, we cast a commonly used chatter model into a Bayesian model updating framework to calibrate its parameters

based on the vibration data acquired during machining. In this framework, chatter model parameters are treated as random processes with a presumed (prior) probability distributions, which are then updated to their (more accurate) posterior distribution based on the new information gained from in-process vibration data. Although the analysis is applicable to cutting force model parameters as well, we only consider the modal parameters and assume the force model is updated separately (e.g. following the method in [5]). The presented new approach offers a number of important advantages over the existing methods. First, only stable vibrations are used in the presented method, while the existing methods require chatter tests performed under both stable and unstable conditions. In a different approach to existing methods, we update the model parameters based on closed-loop system poles rather than experimentally determined chatter limits. The dominant system poles are identified from Operational Modal Analysis (OMA) of stable vibration signals and therefore no chatter encounters are required for model updating with the presented method. Second, the updated probability distributions provide an estimate of uncertainty in model parameters, which can then be used in robust stability analysis methods to determine the confidence levels in chatter predictions [12, 13]. Here, we use second order perturbation analysis to establish credibility bounds around the predictions of the chatter model based on the updated probability distributions of its parameters. Third, model parameters are updated based a limited set of experimental data that can be gathered over time during regular machining operations to adaptively improve chatter predictions. A similar Bayesian approach has recently been presented by Li et al. [14] and Chen et al. [15] for milling, where updating was performed based on the information gained from chatter encounters and not stable machining conditions.

In the next section, modeling chatter in turning operations is discussed. Considering the extensive literature that is available on chatter modeling, Section 2 only presents a high-level description of two models that are used later to formulate the model updating problem and estimate the credibility bounds of stability estimation. In Section 3, second order perturbation method is used to

determine the variance of chatter predictions for a given variance in model parameters. This analysis is then used in Sections 6.2 and 6.4 to select the model parameters to be updated and to develop credibility bounds around chatter predictions. In Section 4, the OMA method developed in [16] is briefly discussed, because the machining system poles that are extracted by this method are used as experimental observations in the Bayesian model updating framework presented in Section 5. Th presented method is used in an experimental case-study in Section 6 to validate its effectiveness in enhancing chatter predictions.

2. Dynamics of Regenerative Chatter in Turning

Consider the turning setup shown in Fig.1. The equation governing the elastic oscillations of the tool in the modal space is expressed as follows:

$$\ddot{\boldsymbol{q}}(t) + 2\boldsymbol{\Omega Z}\dot{\boldsymbol{q}}(t) + \boldsymbol{\Omega^2 q}\,(t) = \boldsymbol{\Phi^T f}\,(t) \tag{1}$$

where $\boldsymbol{q} \in \mathbb{R}^N$ is the vector of modal coordinates, $\boldsymbol{\Phi} = [\boldsymbol{\phi}_1, ..\boldsymbol{\phi}_N] \in \mathbb{R}^{2\times N}$ is the matrix of mass-normalized mode shapes, and $\boldsymbol{Z} = \text{diag}(\zeta_n)$ and $\boldsymbol{\Omega} = \text{diag}(\omega_n)$ are diagonal matrices of modal frequencies and damping ratios, ω_n and ζ_n, $n = 1..N$, respectively. A total number of N modes described by two degrees of freedom, $z_1(t)$ and $y_1(t)$, are considered. Since the tool's deflections in X-direction are negligible and the workpiece deflections in that direction do not affect the chip thickness and thereby chatter stability, vibrations in the X-direction are neglected.

Because modal parameters are usually determined experimentally (e.g. by impulse hammer tests), they include a certain level of uncertainty and variance due to measurement and curve-fitting errors. In addition, the variation of modal parameters under operational conditions further increases their uncertainty. To account for such uncertainties, we assume each of the nominal modal frequencies, damping ratios and mass-normalized mode shapes to be subjected to random

variations, as follows:

$$\begin{aligned} \omega_n &= \bar{\omega}_n(1+\theta_{\omega_n}) \\ \zeta_n &= \bar{\zeta}_n(1+\theta_{\zeta_n}) \\ \boldsymbol{\phi}_n &= \bar{\boldsymbol{\phi}}_n(1+\theta_{\phi_n}) \end{aligned} \tag{2}$$

where the bar symbols denote the nominal values. Mode shapes are assumed to remain unchanged but their mass-normalization constant (i.e. modal mass or stiffness) is subjected to θ_{ϕ_n} variation. Nominal values of modal frequency and damping are similarly subjected to θ_{ω_n} and θ_{ζ_n} random variations, respectively. The goal in this work is to determine the joint probability distribution of the vector of variations $\boldsymbol{\theta}_m = [\theta_{\omega_n}, \theta_{\zeta_n}, \theta_{\phi_n}]^T$ based on the tool vibrations measured during the turning process.

Force vector, $\boldsymbol{f} \in \mathbb{R}^2$, comprises the machining forces at the tool's tip in the feed (Z) and cutting (Y) directions. Linear mechanistic model is used to relate the machining forces to the uncut chip cross-section area, as follows:

$$\boldsymbol{f}(t) = a\boldsymbol{K}_c\boldsymbol{\Phi}\left(\boldsymbol{q}(t-\tau) - \boldsymbol{q}(t)\right) \tag{3}$$

where a is width of cut, τ is spindle rotation period, and the constant matrix $\boldsymbol{K}_c = \begin{bmatrix} k_{fc}, & k_{tc} \end{bmatrix}^T \begin{bmatrix} 1, & 0 \end{bmatrix}$ includes the force coefficients, k_{tc} and k_{fc}, in cutting (tangential) and feed directions, respectively. The term $\boldsymbol{q}(t-\tau) - \boldsymbol{q}(t)$ represents uncut chip thickness modulations due to vibrations in the current and previous spindle rotations, depicted schematically in Fig. 1(a). Tool deflections are measured from static equilibrium and therefore the static components of the forces are neglected. Substituting the forces from Eq.3 in Eq.1 leads to the following delay differential equation which describes the closed-loop dynamics in the machining process:

$$\ddot{\boldsymbol{q}}(t) + 2\boldsymbol{\Omega}\boldsymbol{Z}\dot{\boldsymbol{q}}(t) + \boldsymbol{\Omega}^{\boldsymbol{2}}\boldsymbol{q}\,(t) = a\boldsymbol{\Phi}^T\boldsymbol{K}_c\boldsymbol{\Phi}\left(\boldsymbol{q}(t-\tau) - \boldsymbol{q}(t)\right) \tag{4}$$

Figure 1(c) describes the same closed-loop dynamics in block-diagram form. In the following sections, the two common approaches to determining the stability of this closed-loop system at arbitrary values of cutting width (a) and spindle speed ($\Omega = 2\pi/\tau$) are discussed.

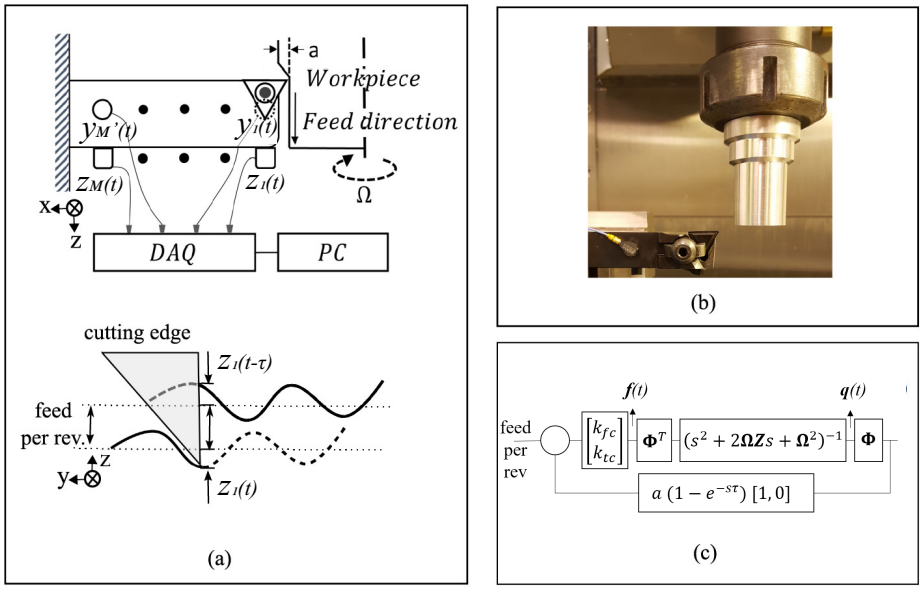

Figure 1: (a) schematic of turning model, (b) Turning Setup, and (c) block diagram of regenerative chatter dynamics in turning [16]

2.1. Frequency-domain method

Characteristic equation of the closed-loop system is obtained by taking Laplace transformation from the two sides of Eq.4:

$$|\boldsymbol{I}s^2 + 2\boldsymbol{\Omega Z}s + \boldsymbol{\Omega^2} - \Phi^T a \boldsymbol{K}_c \boldsymbol{\Phi}\left(e^{-s\tau} - 1\right)| = 0 \tag{5}$$

where $|.|$ stands for matrix determinant and s is Laplace variable. Stability of the closed-loop system is determined by the roots of the characteristic equation, or the system poles, denoted $\lambda(a, \tau, \boldsymbol{\theta}_m) \in \mathbb{C}$. Each pair of complex-conjugate poles is characterized by its frequency, $\omega(a, \tau, \boldsymbol{\theta}_m)$, and damping ratio, $\zeta(a, \tau, \boldsymbol{\theta}_m)$, as follows:

$$\lambda, \lambda^* = -\zeta\omega \pm i\omega\sqrt{1 - \zeta^2)} \tag{6}$$

where the argument $(a, \tau, \boldsymbol{\theta}_m)$ is dropped for notation simplification. The delay term in the feedback loop converts the N-DOF system to a distributed-parameter system with infinite number of poles. For any given values of cutting width (a) and spindle speed $(\Omega = 2\pi/\tau)$, system vibrations are stable if all of

its poles have negative real parts; the system is unstable if any of its poles have a positive real part. By increasing the cutting width at each spindle speed, one pair of complex-conjugate poles, denoted $\lambda_m(a, \tau, \boldsymbol{\theta}_m)$, will cross the imaginary axis from left to right when cutting width reaches its chatter limit, causing Hopf-bifurcation of the static equilibrium, known as chatter.

2.2. Discrete-time-domain method

Discretization methods can be used to approximate the distributed-parameter system in Eq.4 by a lumped-parameter system. The delay differential equation in Eq.4 can be written in the following state-space form:

$$\frac{d}{dt}\begin{Bmatrix} \boldsymbol{q}(t) \\ \dot{\boldsymbol{q}}(t) \end{Bmatrix} = \boldsymbol{A}\begin{Bmatrix} \boldsymbol{q}(t) \\ \dot{\boldsymbol{q}}(t) \end{Bmatrix} + \boldsymbol{B}\begin{Bmatrix} \boldsymbol{q}(t-\tau) \\ \dot{\boldsymbol{q}}(t-\tau) \end{Bmatrix} \tag{7}$$

where

$$\boldsymbol{A} = \begin{bmatrix} \boldsymbol{0} & \boldsymbol{I} \\ -\boldsymbol{\Omega}^2 - \boldsymbol{\Phi}^T a \boldsymbol{K}_c\, \boldsymbol{\Phi} & -2\boldsymbol{\Omega}\boldsymbol{Z} \end{bmatrix}; \boldsymbol{B} = \begin{bmatrix} \boldsymbol{0} & \boldsymbol{0} \\ \boldsymbol{\Phi}^T a \boldsymbol{K}_c \boldsymbol{\Phi} & \boldsymbol{0} \end{bmatrix} \tag{8}$$

By uniformly discretizing one spindle revolution period into m intervals such that $\tau = m\Delta t$, and treating the delay term in Eq.7 in each interval as constant input force to the N-DOF system, the distributed-parameter system is approximated by a lumped-parameter system described by the following state-space equation:

$$\boldsymbol{u}_{i+1} = \boldsymbol{G}(a, \tau, \boldsymbol{\theta}_m)\boldsymbol{u}_i \tag{9}$$

where $\boldsymbol{u}_i = \boldsymbol{u}(i\Delta t) \in \mathbb{R}^{2N(m+1)}$ is the state vector in discrete-time domain and $\boldsymbol{G}(a, \tau, \boldsymbol{\theta}_m) \in \mathbb{R}^{2N(m+1)\times 2N(m+1)}$ is state-transition matrix. Various methods can be employed to discretize the system; we use full-discretization method of Ding et al. due to its high computational efficiency [17]. The state-transition matrix resulting from full-discretization depend on the modal parameters of the system, uncut chip width, and spindle rotation period (see [17] for the detailed

derivations):

$$\boldsymbol{G} = \begin{bmatrix} \mathbf{\Phi}_0 & \mathbf{0} & \mathbf{0} & \cdots & \mathbf{0} & \left(\mathbf{\Phi}_1 - \frac{1}{\Delta t}\mathbf{\Phi}_2\right)\boldsymbol{B} & \frac{1}{\Delta t}\mathbf{\Phi}_2\boldsymbol{B} \\ \mathbf{I} & \mathbf{0} & \mathbf{0} & \cdots & \mathbf{0} & \mathbf{0} & \mathbf{0} \\ \mathbf{0} & \mathbf{I} & \mathbf{0} & \cdots & \mathbf{0} & \mathbf{0} & \mathbf{0} \\ \vdots & \vdots & \vdots & \ddots & \vdots & \vdots & \vdots \\ \mathbf{0} & \mathbf{0} & \mathbf{0} & \cdots & \mathbf{0} & \mathbf{0} & \mathbf{0} \\ \mathbf{0} & \mathbf{0} & \mathbf{0} & \cdots & \mathbf{I} & \mathbf{0} & \mathbf{0} \\ \mathbf{0} & \mathbf{0} & \mathbf{0} & \cdots & \mathbf{0} & \mathbf{I} & \mathbf{0} \end{bmatrix} \tag{10}$$

where

$$\mathbf{\Phi}_0 = e^{\boldsymbol{A}\Delta t}; \mathbf{\Phi}_1 = \boldsymbol{A}^{-1}\left(\mathbf{\Phi}_0 - \boldsymbol{I}\right); \mathbf{\Phi}_2 = \boldsymbol{A}^{-1}(\Delta t\mathbf{\Phi}_0 - \mathbf{\Phi}_1) \tag{11}$$

Eigenvalues of matrix, $\boldsymbol{G}$, determine the system stability. State-transition matrix is real-valued but nonsymmetric; therefore, its eigenvalues, $\mu_j(a, \tau, \boldsymbol{\theta}_m), j = 1..2N(m+1)$, comprise a set of complex conjugate pairs satisfying the following equation:

$$(\mathbf{G} - \mu_j\mathbf{I})\mathbf{u_j} = \mathbf{0}; \mathbf{v_j}^{\mathrm{T}}(\mathbf{G} - \mu_j\mathbf{I}) = \mathbf{0} \tag{12}$$

where $\mathbf{u_j}$ and $\mathbf{v_j}$ are the right and left eigenvectors corresponding to eigenvalue μ_j, assuming $\mathbf{v_j}^T\mathbf{u_j} = 1$ scaling. For any given combination of spindle speed and cutting width, the system is stable if all of the eigenvalues ($\mu_j, j = 1..2N(m+1)$) have modulus smaller than 1, and the system is unstable if the modulus of any of the eigenvalues is greater than 1. By increasing cutting width (a) at a constant spindle speed ($\Omega = 2\pi/\tau$), the static equilibrium of the system ($\boldsymbol{u}_i = 0$) loses stability at the chatter limit. At this point a complex conjugate pair of eigenvalues, denoted $\mu_m(a, \tau, \boldsymbol{\theta}_m)$ and $\mu_m^*(a, \tau, \boldsymbol{\theta}_m)$, exit the unit circle on the complex plane. This dominant discrete-time pole can be regarded as an approximation of its continuous-time counterpart in Section 2.1: $\mu_m(a, \tau, \boldsymbol{\theta}_m) \approx e^{\lambda_m(a,\tau,\boldsymbol{\theta}_m)\Delta t}$.

3. Uncertainty Propagation

Uncertainty in modal parameters, represented by $\boldsymbol{\theta}_m$, propagates to the system poles ($\mu_m(a, \tau, \boldsymbol{\theta}_m)$) and consequently its stability. The goal in this section is to determine the variance in the system poles for a given variance in modal parameters. Since chatter stability is directly determined by the system poles, the resulting pole variance can be used as a proxy for uncertainty in chatter predictions.

Suppose the vector of modal parameter variations $\boldsymbol{\theta}_m$ is a zero-mean Gaussian process with covariance matrix, $\boldsymbol{\Sigma}_\theta$:

$$\boldsymbol{\Sigma}_\theta = \mathbb{E}[\boldsymbol{\theta}_m.\boldsymbol{\theta}_m^T] \tag{13}$$

For sufficiently small $\boldsymbol{\theta}_m$ and fixed a and τ, $\mu_m(a, \tau, \boldsymbol{\theta}_m)$ can be approximated by the second-order perturbation of its value when the nominal modal parameters are used:

$$\mu_m(\boldsymbol{\theta}_m) \approx \mu_m(0) + \boldsymbol{d}_\mu^T \boldsymbol{\theta}_m + \frac{1}{2}\boldsymbol{\theta}_m^T \mathbf{D}_\mu \boldsymbol{\theta}_m \tag{14}$$

where dependency on the fixed a and τ are dropped from notation. Entries of the gradient vector, $\boldsymbol{d}_\mu$, and Hessian matrix, $\mathbf{D}_\mu$, are evaluated at $\boldsymbol{\theta}_m = 0$ and can be expressed in terms of the corresponding eigenvalues and eigenvectors, as follows [18]:

$$\frac{\partial \mu_m}{\partial \theta_k} = \mathbf{v}_m^T \frac{\partial \boldsymbol{G}}{\partial \theta_k} \mathbf{u}_m \tag{15}$$

$$\frac{\partial^2 \mu_m}{\partial \theta_i \partial \theta_j} = \mathbf{v}_m^T \frac{\partial^2 \mathbf{G}}{\partial \theta_i \partial \theta_j} \mathbf{u}_m + \sum_{r=1, r\neq m}^{2N(m+1)} \frac{\left(\mathbf{v}_m^T \frac{\partial \mathbf{G}}{\partial \theta_i} \mathbf{u}_r\right)\left(\mathbf{v}_r^T \frac{\partial \mathbf{G}}{\partial \theta_j} \mathbf{u}_m\right) + \left(\mathbf{v}_m^T \frac{\partial \mathbf{G}}{\partial \theta_j} \mathbf{u}_r\right)\left(\mathbf{v}_r^T \frac{\partial \mathbf{G}}{\partial \theta_i} \mathbf{u}_m\right)}{\mu_m - \mu_r} \tag{16}$$

Nobari et al. derived closed-form expressions for the mean and variance of the perturbed eigenvalue, subjected to the Gaussian distribution of the model parameters [19]:

$$\bar{\mu}_m = \mathbb{E}[\mu_m(\boldsymbol{\theta}_m)] = \mu_m(0) + \frac{1}{2}\text{Trace}(\boldsymbol{\Sigma}_\theta \mathbf{D}_\mu) \tag{17}$$

and

$$\mathbb{E}\left[(\mu_m(\boldsymbol{\theta}_m)-\bar{\mu}_m)(\mu_m(\boldsymbol{\theta}_m)-\bar{\mu}_m)^*\right]=\boldsymbol{d}_\mu^T\boldsymbol{\Sigma}_{\boldsymbol{\theta}}\boldsymbol{d}_{\mu^*}+\frac{1}{2}\text{Trace}(\boldsymbol{\Sigma}_\theta\mathbf{D}_\mu\boldsymbol{\Sigma}_\theta\mathbf{D}_{\mu^*}) \tag{18}$$

In Section 6.2, we will use these expressions to study the sensitivity of stability predictions to modal parameter uncertainties. We will also use these expressions in Section 6.4 to establish credibility bounds around the system's stability diagrams.

4. Operational Modal Analysis

The dominant poles of the closed-loop system in Eq.4 can be identified experimentally by Operation Modal Analysis of the vibration signals measured during turning [16]. While most of common OMA methods could be used for this purpose, we use Mohanty and Rixen's Modified Least Squares Complex Exponential (LSCE) method [20], because it allows for the effective elimination of undamped harmonics from pole identification process. A brief overview of the method is presented here; the details can be found in [16].

The eigenvalues (poles) of the lumped system in Eq.9, are the roots of its characteristic polynomial:

$$\beta_0+\beta_1\mu_j^1+\beta_2\mu_j^2+\cdots+\beta_{2P-1}\mu_j^{2P-1}+\mu_j^{2P}=0 \tag{19}$$

where $\beta_0,\beta_1,...,\beta_{2P}$, are the coefficients of the characteristic polynomial and P is the assumed system order. The appropriate order is determined using stabilization diagrams as explained in [16]. In addition to system poles, characteristic polynomial in Eq.19 also admits the Correlation Function (CF) of the acceleration signals measured under (random) operational loads [21]:

$$\beta_0\mathbf{r}_y(i)+\beta_1\mathbf{r}_y(i+1)+\beta_2\mathbf{r}_y(i+2)+\cdots+\beta_{2P-1}\mathbf{r}_y(i+2P-1)=-\mathbf{r}_y(i+2P) \tag{20}$$

For accelerations measured by M accelerometers in $Z-$direction and M' accelerometers in $Y-$direction, as shown in Fig.1(a), each entry of the vector

$\mathbf{r}_y(i)$ is the CF of one of the $M + M'$ acceleration signals with respect to the reference signal (designated y_0). The CF is directly estimated by the following summation, while other methods could also be used to estimate them [22]:

$$\mathbf{r}_y(i) = \frac{1}{(L-i)} \sum_{k=1}^{L-i} \mathbf{y}(k) y_0(k+i); i = 0 \cdots L-1 \tag{21}$$

where L is the length of the recorded signal and $\mathbf{y}(i) = [y_1(i)\ ,\ y_2(i)\ ,\ ..\ ,\ y_M(i)\ ,\ z_1(i)\ ,\ z_2(i)\ ,\ ..\ ,\ z_{M'}(i)]^T$ is the vector of accelerations measured by the $M + M'$ sensors.

Vibration signals measured during turning include the transient response of the tool to random machining forces as well as its forced response to harmonic machining forces at the spindle rotation frequency. Because the harmonic component of the response usually includes much higher energy, the identification process will naturally detect many undamped poles at the harmonics of spindle rotation frequency. Therefore, even when the structural modes are identified by high-order models, their accuracy is affected by those harmonic poles. To compensate for the effect of harmonic response, Mohanty and Rixen [20] proposed to treat the harmonic frequencies as known undamped system poles (purely imaginary eigenvalues), which would also satisfy the characteristic polynomial in Eq.19. Repeating Eq. 20 for np consecutive time steps, and combining the resulting equations with the ones obtained by substituting the undamped poles (known harmonics) in the characteristic polynomial, leads to the following system of algebraic equations:

$$\mathbf{E}_1 \mathbf{b}_1 + \mathbf{E}_2 \mathbf{b}_2 = \mathbf{f}_1 \tag{22}$$

and

$$\mathbf{E}_3 \mathbf{b}_1 + \mathbf{E}_4 \mathbf{b}_2 = \mathbf{f}_2 \tag{23}$$

where $\begin{bmatrix} \beta_0 & \cdots & \beta_{2P-1} \end{bmatrix} = \left[{\mathbf{b}_1}^T, {\mathbf{b}_2}^T \right]$, and the components of $\mathbf{E}_{1,2,3,4}$ and $\mathbf{f}_{1,2}$ are discrete time CF values and discrete sinusoidal functions of the harmonic terms. The components of these matrices are provided in Appendix. Eq.20 must be exactly satisfied to enforce the known harmonic poles. This equation

is therefore solved to obtain $\mathbf{b}_1$, which is then substituted in Eq.22 to develop the following over-determined system of equations:

$$\left(\mathbf{E}_2 - \mathbf{E}_1\mathbf{E}_3^{-1}\mathbf{E}_4\right)\mathbf{b}_2 = \mathbf{f}_1 - \mathbf{E}_1\mathbf{E}_3^{-1}\mathbf{f}_2 \tag{24}$$

Least squares approximation of $\mathbf{b_2}$ from Eq.24 along with the corresponding solution of $\mathbf{b_1}$ form the complete solution of the coefficients of the characteristic polynomial, $\beta_0, ..., \beta_{2P-1}$. Subsequently, poles of the discrete-time domain system are obtained as the roots of the characteristic polynomial. The total $2P$ roots of the polynomial include the considered harmonic terms as well as the damped poles of the system as pairs of complex conjugate roots. The estimated dominant pole, $\hat{\mu}_m$ is the structural pole with the largest modulus. The $\hat{.}$ sign designates the estimated value of the theoretical value– for example, $\hat{\mu}_m$ is the experimental estimation of μ_m.

Having identified the dominant pole of the discrete-time-domain system, one can estimate the equivalent continuous-time pole as $\hat{\lambda}_m = \frac{\ln \hat{\mu}_m}{T_s}$, with T_s being the measurement sampling time. This continuous-time pole is regarded as an estimation for the dominant root (λ_m) of the characteristic equation (Eq.5) in the frequency-domain model. According to Eq.6, the frequency ($\hat{\omega}_m$) and damping ratio ($\hat{\zeta}_m$) of each identified pole are obtained from its real parts ($\Re(\hat{\lambda}_m)$) and modulus ($\sqrt{\hat{\lambda}_m\hat{\lambda}_m^*}$) as follows:

$$\begin{aligned} \hat{\omega}_m &= \sqrt{\hat{\lambda}_m\hat{\lambda}_m^*} \\ \hat{\zeta}_m &= \frac{-\Re(\hat{\lambda}_m)}{\hat{\omega}_m} \end{aligned} \tag{25}$$

In the following sections, the described OMA process will be conducted to identify the dominant continuous-time pole or its associated damping and frequency at N_r distinct combinations of spindle speeds and cutting width. The identification process at each point is also repeated N_s times. Therefore, the general index m is replaced by indeces $r = 1..N_r$ and $j = 1..N_s$ to denote the dominant closed-loop pole ($\hat{\lambda}_{rj}$) and its frequency and damping ($\hat{\omega}_{rj}$ and $\hat{\zeta}_{rj}$) when $a = a_r$ and $\tau = \tau_r$.

Notation convention: We use ω and ζ to denote both modal (Eq.1) and closed-loop frequency and damping ratios (Eqs.6 and 25). Modal parameters,

which are assumed to be independent from a and τ, are identified by the index $n = 1..N$. Closed-loop frequency and damping ratio values, which vary by cutting width and spindle speed, are identified by the argument $(a, \tau, \boldsymbol{\theta})$ or the index $r = 1..N_r$.

5. Bayesian Model Updating

Bayesian Model Updating employs Bayes' theorem to update the prior joint probability distribution of model parameters ($\boldsymbol{\theta}$) to their posterior joint distribution based on a set of experimental observation. Model parameters in this work comprise $\boldsymbol{\theta}_m$ and the variance of model prediction errors, as will be explained in Section 5.1. The general Bayes' theorem adopted for updating the parameters of model class $\mathcal{M}$ is expressed as follows[23]:

$$p(\boldsymbol{\theta} \mid \boldsymbol{D}, \mathcal{M}) = \frac{p(\boldsymbol{D} \mid \boldsymbol{\theta}, \mathcal{M}) p(\boldsymbol{\theta} \mid \mathcal{M})}{p(\boldsymbol{D} \mid \mathcal{M})} \tag{26}$$

In our application of this theory, the data vector, $\boldsymbol{D} = \left[\hat{\lambda}_1, ..., \hat{\lambda}_{N_r}\right]^T$, comprises the dominant closed-loop poles obtained from the OMA of vibration signals measured at N_r distinct combinations of width of cut and spindle speed. The prior distribution of model parameters, $p(\boldsymbol{\theta}|\mathcal{M})$, is selected based on a prior knowledge of the uncertainty distribution over each model parameter. For instance, when hammer test results are available, the prior distribution for each modal parameter can be assumed Gaussian centred at the value identified from modal testing with variance proportional to the presumed uncertainty of that parameter. The prior PDF can also be uniform over a range of values that are known based on past experiences or numerical and analytical models. The likelihood function, $p(\boldsymbol{D}|\boldsymbol{\theta}, \mathcal{M})$, is the joint distribution of the observed data given a specific set of model parameters; therefor, the formulation of this function depends on the model being updated. In the following section, the likelihod function will be formulated based on the chatter model discussed in Section 2. The denominator of Eq.26 is the marginal distribution of the observed data, also known as

evidence:

$$p(\boldsymbol{D} \mid \mathcal{M}) = \int p(\boldsymbol{D} \mid \boldsymbol{\theta}, \mathcal{M}) p(\boldsymbol{\theta} \mid \mathcal{M}) d\boldsymbol{\theta} \tag{27}$$

Evidence for each model class $\mathcal{M}$ is a constant that normalizes the posterior parameter distribution. Computing the model evidence and its importance in selecting a proper model class ($\mathcal{M}$) will be discussed in Sections 5.2and 5.3

5.1. Likelihood Function

Poles of the close-loop system must satisfy its characteristic equation in Eq.5. Because of modeling, measurement, and identification errors, the poles identified by OMA will produce a residual error once substituted in the characteristic equation:

$$|\boldsymbol{I}\hat{\lambda}_{rj}^2 + 2\boldsymbol{\Omega Z}\hat{\lambda}_{rj} + \boldsymbol{\Omega^2} - \boldsymbol{\Phi}^T a_r \boldsymbol{K}_c \boldsymbol{\Phi} \left(e^{-\hat{\lambda}_{rj}\tau_r} - 1 \right)| = e_{Rrj}(\boldsymbol{\theta}_m) + i e_{Irj}(\boldsymbol{\theta}_m) \tag{28}$$

where $\boldsymbol{\Omega}, \boldsymbol{Z}$ and $\boldsymbol{\Phi}$ are functions of $\boldsymbol{\theta}_m$, as indicated in Eqs.1 and 2, and e_{Rrj} and e_{Irj} are the real and imaginary parts of the residual error. To avoid large numbers, which might affect the numerical efficiency of the updating process, we normalize e_{Rrj} and e_{Irj} by their average values at $\boldsymbol{\theta}_m = \boldsymbol{0}$ and denote the normalized values $\bar{e}_{Rrj}(\boldsymbol{\theta}_m)$ and $\bar{e}_{Irj}(\boldsymbol{\theta}_m)$. Based on the Principle of Maximum Entropy [24, 25] the normalized residual error components are assumed to be statistically independent zero-mean random processes with Gaussian distribution:

$$p(\bar{e}_{Rrj}, \bar{e}_{Irj}) = \mathcal{N}\left(\begin{bmatrix} 0 \\ 0 \end{bmatrix}, \begin{bmatrix} \sigma_R^2 & 0 \\ 0 & \sigma_I^2 \end{bmatrix} \right) \tag{29}$$

where σ_R and σ_I are standard deviations of normalized errors. Note that the residual errors represent a combination of modeling, measurement, and identification errors. Since the residual errors from each of the $N_r \times N_s$ identified poles are assumed statistically independent from others, likelihood function can be defined as the product of the Probability Distribution Functions (PDF) of the residual errors from each of the poles:

$$p(\boldsymbol{D}|\boldsymbol{\theta}_m, \sigma_R, \sigma_I) = c_1 \exp\left(-\frac{1}{2} \sum_{j=1}^{N_s} \sum_{r=1}^{N_r} \left(\frac{\bar{e}_{Rrj}^2(\boldsymbol{\theta}_m)}{\sigma_R^2} + \frac{\bar{e}_{Irj}^2(\boldsymbol{\theta}_m)}{\sigma_I^2} \right) \right) \tag{30}$$

where $c_1^{-1} = (2\pi\sigma_R\sigma_I)^{(N_r+N_s)}$ is the normalizing constant of the joint PDF. The values of σ_R and σ_I determine the weight of contributions from the real and imaginary parts of residual errors to the likelihood function and consequently the posterior distribution of the model parameters. For instance, if σ_R is much smaller than σ_I, the updated posterior distribution is dominated by the real part of the residual error and the information in the imaginary part will be mostly disregarded. Therefore, extracting the maximum possible information from the experimental data requires a balanced contributions from both the real and imaginary parts of residual errors. Such a balance is controlled by introducing a new coefficient α such that $\sigma_I^2 = \alpha\sigma_R^2$, where $\alpha \in \{\alpha_1, \alpha_2, ..., \alpha_K\}$ is selected from a set of discrete values each defining a new model class $\mathcal{M}_k = \mathcal{M}(\alpha_k)$ with a different contribution weight from the real and imaginary parts of error. The variance of real residual error, σ_R^2, is treated as an additional model parameter and its distribution is updated with the rest of model parameters; therefore $\boldsymbol{\theta} = [\boldsymbol{\theta}_m, \sigma_R^2]^T$. The optimum model class is selected by a secondary Bayesian updating process as will be explained in Section 5.2. Ultimately, the likelihood function associated with the chatter model is expressed as follows:

$$p(\boldsymbol{D}|\boldsymbol{\theta}, \mathcal{M}_k) = c_1 \exp\left(-\frac{1}{2}\sum_{j=1}^{N_s}\sum_{r=1}^{N_r}\left(\frac{\bar{e}_{Rrj}^2(\boldsymbol{\theta}_m)}{\sigma_R^2} + \frac{\bar{e}_{Irj}^2(\boldsymbol{\theta}_m)}{\alpha\sigma_R^2}\right)\right) \tag{31}$$

5.2. Model class selection

Denominator in Eq.26, as defined in Eq.27, is known as model evidence or marginal likelihood. Each arbitrarily value of α_k in Eq.31 defines a new model class, $\mathcal{M}_k$, that produces its corresponding marginal likelihood, $p(\boldsymbol{D}|\mathcal{M}_k)$, when substituted in Eq.27. In evidence-based model class selection, a secondary Bayesian updating is performed to determine the probability (plausibility) of each model class in the set $\mathbf{M} = \{\mathcal{M}_1..\mathcal{M}_K\}$ describing the observed data [26, 27]:

$$p\left(\mathcal{M}_k \mid \boldsymbol{D}, \mathbf{M}\right) = \frac{p\left(\boldsymbol{D} \mid \mathcal{M}_k\right) p\left(\mathcal{M}_k \mid \mathbf{M}\right)}{p(\boldsymbol{D} \mid \mathbf{M})} \tag{32}$$

According to Eq.32, if all of the model classes are assigned similar (uniform) prior probabilities, the posterior probability of each model class is proportional

to their evidence, $p(\boldsymbol{D} \mid \mathcal{M}_k)$. The natural logarithm of model evidence, also known as log marginal likelihood, is commonly used to select the model class. Model evidence comprises measures of the data-fitting capabilities of the model and its complexity. This is readily understood from the expansion of log marginal likelihood in the following form [26, 27]:

$$\ln\left[p\left(\boldsymbol{D} \mid \mathcal{M}_k\right)\right] = \mathbb{E}\left[\ln\left[p\left(\boldsymbol{D} \mid \boldsymbol{\theta}, \mathcal{M}_k\right)\right]\right] - \mathbb{E}\left[\ln \frac{p\left(\boldsymbol{\theta} \mid \boldsymbol{D}, \mathcal{M}_k\right)}{p\left(\boldsymbol{\theta} \mid \mathcal{M}_k\right)}\right] \tag{33}$$

where expectations are defined based on the posterior distribution of model parameters. The first term in Eq.33 shows the data-fitting capacity of the model and the second term shows the level of information extracted from the available data, which is correlated with model complexity. The model class with the maximum evidence among the compared model classes is not necessarily the one with a better data-fitting capacity; it is a balanced model with proper data-fitting capacity that is also not too complex; therefore, it is more generalizable.

5.3. Transitional Markov Chain Monte Carlo Sampling

Having defined the likelihood function, we are now able to substitute it in Eq.26 to update the prior distribution of the model parameters to their posterior. However, computing the multivariate integral ($\int p(\boldsymbol{D} \mid \boldsymbol{\theta}, \mathcal{M}) p(\boldsymbol{\theta} \mid \mathcal{M}) d\boldsymbol{\theta}$) in the denominator of the equation can become intractable, especially when a large number of model parameters are to be updated and the likelihood function is sharply peaked. For this reason, instead of solving Eq.26 to obtain the posterior distribution, a numerical algorithm is used to generate samples from the posterior distribution without needing the normalizing constant in the denominator of the equation. As a commonly used method, Markov Chain Monte Carlo (MCMC) algorithm starts from a set of samples drawn from the parameters' prior distribution and generates samples from their posterior. Transitional Markov Chain Monte Carlo (TMCMC) does the same but through an iterative algorithm that is more suitable when posterior distribution is sharply peaked. More importantly, TMCMC also produces the evident (marginal likelihood) of the model, which is then used for model class selection as explained in the previ-

ous section. In this work, we use the improved TMCMC (iTMCMC) algorithm developed by Betz et al. [28] to sample from the posterior PDF of the model parameters and use the produced model evidence to select the most plausible model class among a set of candidates.

6. Experimental Results

The experimental setup shown in Fig.1 was used in [16] to identify the dominant closed-loop poles of the turning system by OMA. The same setup and measured vibrations are used here to demonstrate the implementation and effectiveness of the presented method in updating the chatter model parameters.

The turning setup comprises a tool with square cross-section (19 × 19 mm) mounted on the table of a 3-axis CNC machine and a cylindrical workpiece (38 mm diameter) mounted in the machine's spindle (51 mm overhang). The tool is fed in Z-direction at 0.05 mm/rev and its cutting edge is perpendicular to both feed and cutting directions. Tool's vibrations during turning operations are measured using four piezoelectric accelerometers (PCB 352C22) installed on the tool's shank. Two ($M = 2$) of the accelerometers are installed in Z-direction and the other two ($M' = 2$) in Y-direction. In each direction, one accelerometer was mounted close to the tool tip and the second one 38 mm away from it on the tool's shank. Cutting force coefficients were determined from orthogonal cutting database for Aluminum 6061 [29]: k_{tc}=635 MPa and k_{fc}=159 MPa. More details about the conducted experiments can be found in [16].

The parameters of the dominant vibration modes of the tool identified by impulse hammer tests are shown in Table 1. The first (1842 Hz) and second (2445 Hz) modes predominantly comprise bending deflections in Z and Y directions, respectively. Nonetheless, because both of the modes show significant torsional deflections as well, both of them affect the chip thickness and chatter stability.

The identified modal model can be used in either of the frequency-domain and discrete-time-domain methods discussed in Sections 2.1 and 2.2 to deter-

mine the maximum stable width of cut at each spindle speed. The results are presented in the form of Stability Lobe Diagrams (SLD) shown in Fig.2. Also shown in this figure are the experimentally determined stable and unstable points as circles (stable) and crosses (unstable). While the experimental observations agree with the SLD predictions at 7500 rev/min and 7150 rev/min spindle speeds, the maximum stable cutting width is over-estimated by about 30% at 7300 rev/min. In this section, we use the stable vibration signals measured at points P1-P5 shown in Fig.2 to update the tool's modal parameters, expecting to achieve a closer agreement between the predicted and observed maximum stable cutting width at all of the tested spindle speeds. We also use the experimental observations to estimate the uncertainty in the updated modal parameters and establish credibility bounds around the SLD.

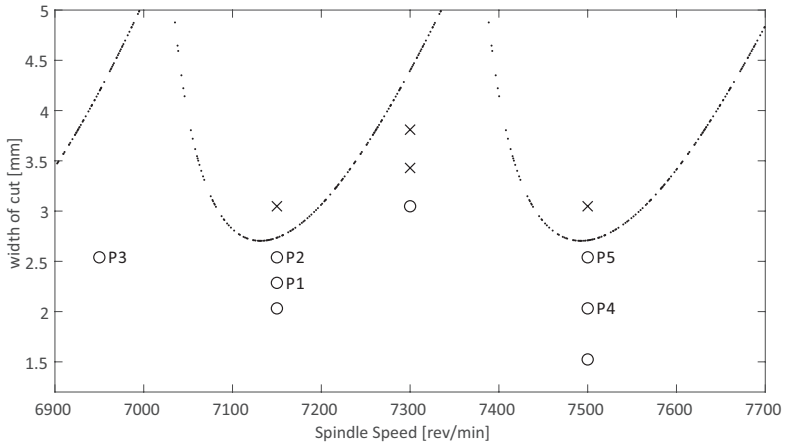

Figure 2: Stability Lobe Diagrams obtained based on the impulse hammer test results, and experimentally observed stable (circles) and unstable (crosses) points

6.1. OMA of stable vibration signals

Modified LSCE method was used for the OMA of the stable vibration signals measured at points P1-P5 shown in Fig.2. The details of measurements and analysis can be found in [16]. At each point, OMA was repeated N_s=10 times by randomly selecting a portion of the recorded vibration signals each time.

Table 1: Modal parameters of the turning tool, obtained from impulse hammer tests

Mode (n)	$\omega_n/2\pi$ [Hz]	ζ_n	$\phi_n[z_1, y_1]$
1	1842	0.021	[2.8,-0.9]
2	2445	0.009	[0.9,2.6]

Stabilization diagram for one of the ten repetitions at point P2 is shown in Fig.3 (a), where the dominant pole and three of its neighbouring harmonic poles (with zero damping) are identified by the modified LSCE method. Parts b and c of the figure show the variation of the mean and standard deviation of the identified pole's damping and frequency by the model order in all of the ten repetitions. As shown in this figure, at sufficiently high model orders, the identified pole's damping and frequency converge to a constant value. For instance, at point P2, model order 25 was deemed sufficient for identification. Using this model order, the mean and standard deviation of the frequency and damping ratio of the pole identified at all ten repetitions were determined and shown in Table2. Similar process was conducted at P1-P5 (corresponding to $r = 1..5$) and the mean and standard deviations of the identified frequency and damping ratio values are also shown in Table 2. These identified poles are used for model updating in Section6.3.

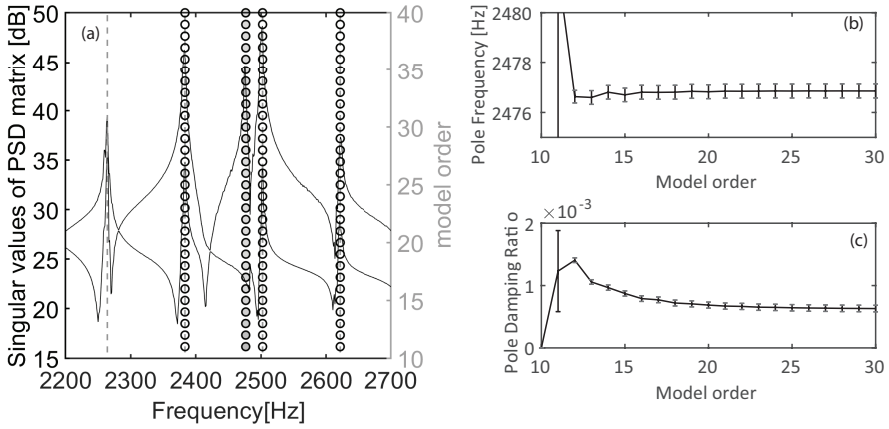

Figure 3: (a) modified LSCE stabilization diagram for point P2, fill-colors of the circles are proportional to the damping ratio of the pole and spindle rotation harmonics are indicated by dashed lines. Only the first two out of the four singular values of the Power Spectral Density (PSD) matrix are shown because the other two are negligible (b and c) variation of the mean and standard deviation (error bars) of the identified pole frequency and damping by model order. Details of analysis are provided in [16]

Table 2: frequency and damping ratios of closed-loop poles identified at each one of the five tested points P1-P5, corresponding to $r = 1..5$

r	$30\Omega/\pi$ [rev/min]	a [mm]	$\hat{\omega}_r/2\pi$ [Hz]	$\hat{\zeta}_r$ $[10^{-2}]$
1	7150	2.286	2473±0.56	0.12±0.014
2	7150	2.54	2477±0.28	0.06±0.005
3	6950	2.54	2508±0.30	0.19±0.007
4	7500	2.032	2476±0.33	0.09±0.005
5	7500	2.54	2476±0.39	0.02±0.004

6.2. Sensitivity Analysis

Sensitivity of the system poles (eigenvalues) to variances in the modal parameters is studied in this section to select the modal parameters that could be updated to improve chatter prediction accuracy. Sensitivities of the dominant

pole (eigenvalue) at each of P1-P5 points are determined from Eq.15 and shown in Table 3.

The eigenvalue variances shown in Table 3 indicate that the closed-loop poles

Table 3: Sensitivity of the dominant pole at P1-P5 to variation in each of the modal parameters

	P1	P2	P3	P4	P5
$\theta\omega_1$	0.0001	0.0002	0.0003	0.0001	0.0001
$\theta\omega_2$	0.3105	0.3025	0.2753	0.3126	0.2955
$\theta\zeta_1$	3.9E-6	4.2E-6	9.8E-6	3.2E-6	3.7E-6
$\theta\zeta_2$	0.0028	0.0028	0.0025	0.0028	0.0027
$\theta\phi_1$	0.0001	0.0001	0.0003	0.0001	0.0001
$\theta\phi_2$	0.0078	0.0080	0.0122	0.0071	0.0075

at points P1-P5 are mainly affected by the parameters of the second mode at 2445Hz and the effect of mode 1 parameters is negligible. Therefore, in the next section, we only consider θ_{ω_2}, θ_{ζ_2}, θ_{ϕ_2} as the modal parameters to update.

6.3. Model updating

The prior PDF of θ_{ω_2} is assumed to be zero-mean normal with 0.001 variance and truncated at ± 0.03. The truncation limits of this parameter correspond to the stability lobes shifting to the left or right by one lobe number. A wider range would admit similar solutions corresponding to higher or lower lobe numbers. The prior PDF of θ_{ζ_2} and θ_{ϕ_2} are also assumed zero-mean normal but with a greater variance of 0.05 and wider truncation limits of ± 0.8. A larger variance was selected for these parameters compared to θ_{ω_2} because the identification of mode shape and modal damping from modal testing is usually more uncertain than modal frequency. Besides, modal damping and stiffness vary more significantly under operational conditions (e.g. due to nonlinearities and process damping). The prior PDF of model prediction error variance is assumed uniform in the range $10^{-10} \leq \sigma_R^2 \leq 0.1$.

A set of 16 model classes with $\alpha_k \in \{2^{-5.5}, 2^{-5.0}, .., 2^2\}$, are considered. For each model class, 5000 samples were generated from the posterior distribution of the model parameters using iTMCMC algorithm. The resulting log marginal likelihood (evidence) for each model class is shown in Fig.4. According to Eq.31, for very small values of α_k, likelihood function is mainly dominated by the prediction error for the imaginary part of characteristic equation and therefore information included in the real part is not extracted. Moreover, according to the same equation, data-fitting capacity of the model is very low for excessively small values of α_k; therefore, both terms in Eq.33 start from vary small values when α_k is small. Data-fitting capacity increases rapidly by increasing α_k until the knee of the curve in Fig.4(a). At this point, contribution weights from the real and imaginary parts to the likelihood function become better balanced, leading to more information extraction from observed data and thus an increasing second term in Eq.33, which penalizes the model for its increased complexity. At α_k=0.5, evidence reaches its maximum, after which it reduces slowly due to the increased model complexity and reduced data-fitting. Part (b) of Fig.4 shows the posterior distribution of the model classes obtained from the secondary Bayesian updating in Eq.32. The model class with α_k=0.5 is selected as the most plausible according to the observed data.

The 25000 samples drawn by iTMCMC from the prior and posterior distributions of model parameters for the model class with α_k=0.5 are shown in Fig.5. This figure shows the samples in 2D planes of model parameters as well as the histograms of the samples for each model parameter, which represents their marginal posterior distributions. According to the drawn samples, the uncertainty of model parameters (represented by their selected prior distributions) is considerably reduced after updating. The variance of each parameter in the posterior distribution is proportional to the sensitivity of the model to that parameter, as discussed in Section 6.2. Since the model is much more sensitive to modal frequency, the marginal distribution of θ_{ω_2} is much more sharper than θ_{ζ_2} and θ_{ϕ_2}. Because the model is not very sensitive to modal damping, the posterior PDF of θ_{ζ_2} has the highest variance among the three modal parameters.

The expected values (mean) of modal frequency increases by 0.67% after updating, which is within the typical curve fitting and measurement errors in modal testing. The expected value of modal damping also increases by 14%, which can be explained due to added process damping at the tested cutting speed range. Expected value of mode shape mass-normalization constant, which represents modal stiffness, also increases by 5.6%.

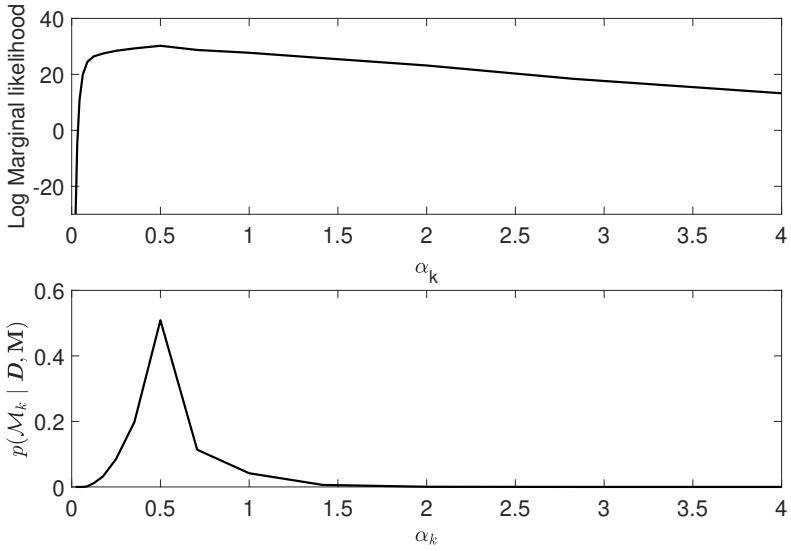

Figure 4: (a) Model marginal likelihood (evidence) for model classes defined by $\alpha_k \in \{2^{-5.5}, 2^{-5.0}, .., 2^2\}$, and (b)Conditional probability of the model classes describing the observed data

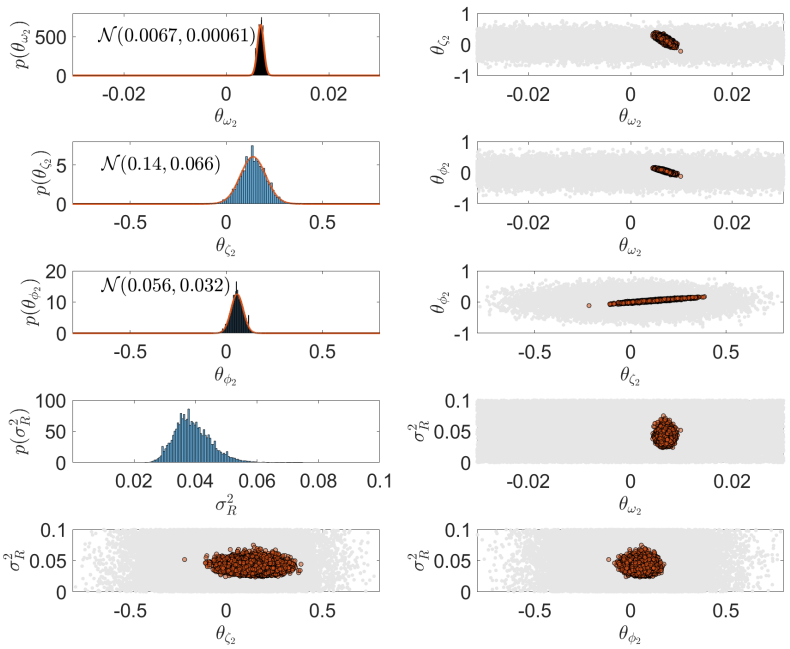

Figure 5: Samples drawn from prior (gray points) and posterior (dark points) distributions of the model parameters for α_k=0.5

In order to demonstrate the effect of α_k on the resulting posterior distributions, the samples drawn from the prior and posterior distributions of model parameters when $\alpha_k = 2^{20}$ is shown in Fig.6. The error in predicting the imaginary part of characteristic equation does not contribute to the likelihood function when α_k is very large. Because the information required to update the modal damping is mainly included in the imaginary part of the characteristic equation, θ_{ζ_2} is not updated and its posterior distribution remains almost equal to its prior distribution.

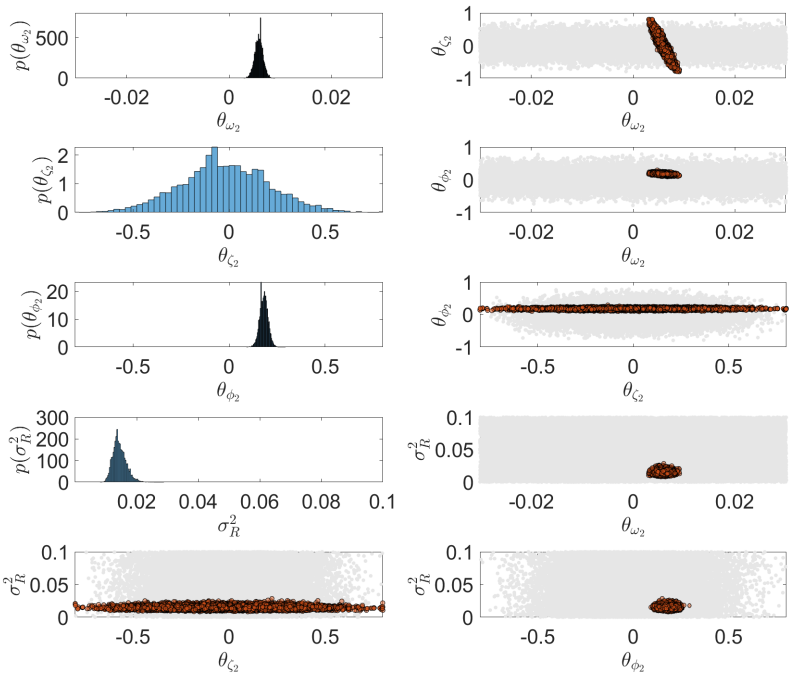

Figure 6: Samples drawn from prior (gray points) and posterior (dark points) distributions of the model parameters for $\alpha_k = 2^{20}$

6.3.1. Uniform prior distribution

In this section, assuming that no or limited prior knowledge of the modal parameters is available, we consider uniform prior PDF for the modal frequency, damping, and mode shape parameters, as shown in Fig.7. This case, for example, could represent a situation where just a limited knowledge of the modal parameters is available via Finite Element Models or user experience. Similar to the previous section, the posterior distributions of $\theta_{\omega_2}, \theta_{\zeta_2}, \theta_{\phi_2}$ are then obtained and displayed in Fig.7. As shown in this figure, with uniform prior distributions, all three parameters converge to posterior distributions that are similar to those obtained from normal priors in Fig.5. The biggest different between the two posterior distributions are observed in the damping parameter,

which is justified due to the lower sensitivity of the model to damping uncertainties, i.e. more data is required to further reduce the uncertainty of the damping parameter. Notice that, in this example, model parameters and their uncertainties were obtained without conducting modal testing. This indicates a potential for eliminating the need for modal testing from the process of determining SLD when sufficient data is available from vibrations gathered during machining.

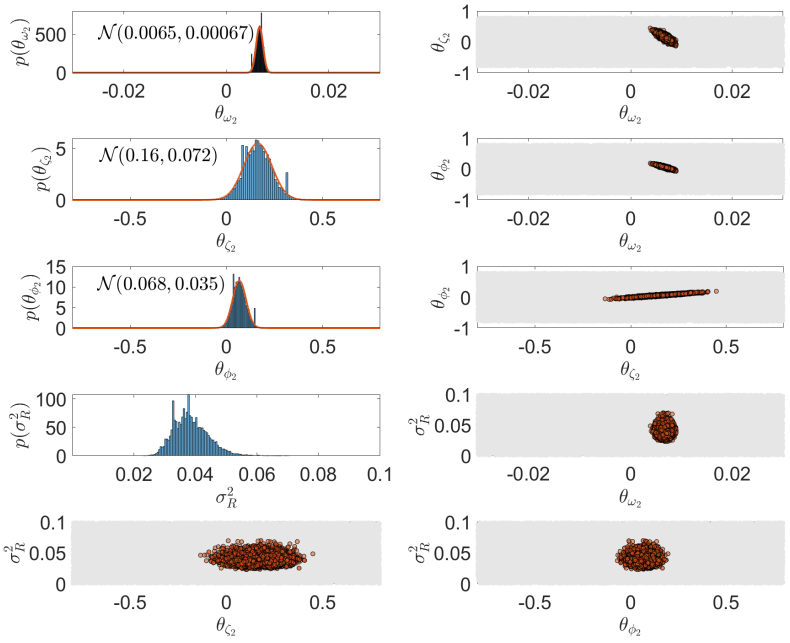

Figure 7: Samples drawn from the *uniform* prior (gray points) and updated posterior (dark points) distributions of the model parameters for α_k=0.5

6.4. SLD with credibility bounds

The posterior distributions shown in Figs.5 are not Gaussian, but one can fit a Gaussian PDF to the marginal distributions of the updated modal parameters. For instance, the Gaussian PDF fitted to the posterior distributions resulting from normal and uniform priors are shown in 5 and 7, respectively. Similarly, mean of the multivariate Gaussian distribution estimated from the posterior

samples shown in Fig. 5 is $\mathbb{E}[\theta_{\omega_2}, \theta_{\zeta_2}, \theta_{\phi_2}] = [0.0067, 0.1385, 0.0549]$, and its covariance matrix is

$$\mathbf{\Sigma}_\theta = \begin{bmatrix} 3.5 \times 10^{-7} & -2.9 \times 10^{-5} & -1.5 \times 10^{-5} \\ -2.9 \times 10^{-5} & 0.0042 & 0.0019 \\ -1.5 \times 10^{-5} & 0.0019 & 9.4 \times 10^{-4} \end{bmatrix} \tag{34}$$

In this section, we use this estimation of the updated parameter distribution to establish the SLD and the 95% credibility bounds around it. To this end, we construct a uniform grid of points on the spindle speed and cutting width plane and determine the magnitude of the largest eigenvalue of the transition matrix at each point. We also determine the variance of the eigenvalue subjected to the model parameter variances from Eq.18. The expected (mean) value of the SLD is the contour plot of the eigenvalues with unit modulus. The upper/lower credibility bounds are determined by the contour plot of the eigenvalues plus/minus one standard deviation equal to unity. Figure 8 shows the resulting SLD and its credibility bounds.

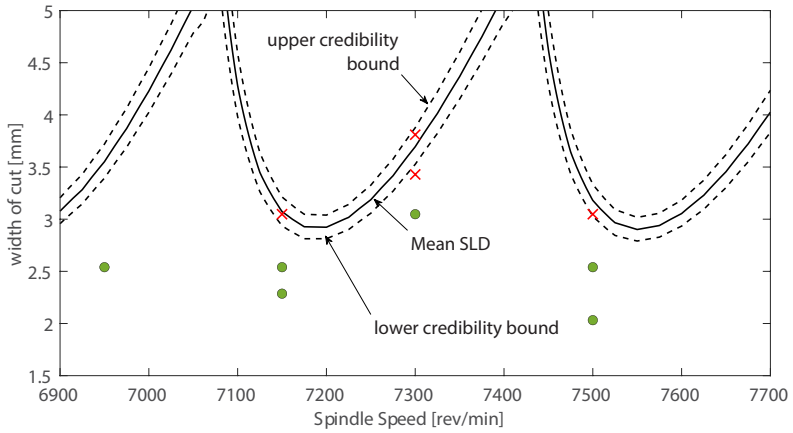

Figure 8: Stability lobe diagrams and their 95% credibility bounds obtained using the model parameters with posterior distributions shown in Fig.5

Compared to the SLD shown in Fig.2, stability borders at all of the tested spindle speeds are predicted accurately after updating model parameters. This

includes the stability at 7300 rev/min, which was predicted incorrectly by the initial SLD based on hammer test results. Furthermore, credibility bounds are now established around the SLD to provide a more informative picture of stability predictions to the process planner. All of the stable points are below the lower credibility bounds of SLD, and all of the unstable points are above or adjacent to them. Notice that the stable point at 7300 rev/min and none of the unstable points were used in model updating but they are predicted correctly by the updated model, confirming its generalizability.

7. Conclusions

Modal parameters in a turning chatter model were updated based on the vibration signals measured during stable machining conditions. In addition to increasing the accuracy of the chatter model, the applied Bayesian framework also provides an estimate of uncertainty about updated modal parameters and thereby the predicted chatter limits.

From computational point of view, the presented method is fast enough for updating the model parameters in practice. The most time-consuming part of the process is the OMA of the measured signals, which can be automated up to some extent. Once the OMA is completed, model parameter updating can be completed within a reasonable time. For example, in the case study in Section 6, generating 5000 samples from posterior distributions with iTMCMC algorithm takes less than two minutes on a consumer-grade computer. Nonetheless, computation time will increase proportionally for models with more parameters.

This paper focused on updating chatter models for turning, but the presented approach could also be adopted for other machining operations such as milling. The main difficulty in such extension would be in the identification of system poles by OMA. System dynamics in turning is Linear Time Invariant but it becomes Linear Time Periodic in milling. If the periodic dynamics is neglected in milling, for example by using Altintas and Budak's zero-order approximation [30], the presented method can be equally applied to milling as well.

Acknowledgement

This research was conducted during the author's study leave at the Institute for Machine Tools and Industrial Management (iwb) at the Technical University of Munich (TUM). I thank Prof. Michael Zaeh and the iwb colleagues for their support.

8. Appendix

8.1. Matrices of Modified LSCE method

Consider m harmonic terms with $\omega_1 ... \omega_m$ rotational frequencies in the vibration signals measured at T_s sampling periods. The components of $\mathbf{E}_{1,2,3,4}$ and $\mathbf{f}_{1,2}$ in Eqs.22 and 23 are expressed in terms of the CF of the measured signals, as follows:

$$
\begin{aligned}
\mathbf{E}_1 &= \begin{bmatrix} \mathbf{r}_y(0) & \cdots & \mathbf{r}_y(2m-1) \\ \vdots & \cdots & \vdots \\ \mathbf{r}_y(np-1) & \cdots & \mathbf{r}_y(np+2m-2) \end{bmatrix} \\
\mathbf{E}_2 &= \begin{bmatrix} \mathbf{r}_y(2m) & \cdots & \mathbf{r}_y(2P-1) \\ \vdots & \cdots & \vdots \\ \mathbf{r}_y(np+2m-1) & \cdots & \mathbf{r}_y(np+2P-2) \end{bmatrix} \\
\mathbf{E}_3 &= \begin{bmatrix} 0 & \cdots & \sin(\omega_1(2m-1)T_s) \\ 1 & \cdots & \cos(\omega_1(2m-1)T_s) \\ \vdots & \cdots & \vdots \\ 0 & \cdots & \sin(\omega_m(2m-1)T_s) \\ 1 & \cdots & \cos(\omega_m(2m-1)T_s) \end{bmatrix} \\
\mathbf{E}_4 &= \begin{bmatrix} \sin(\omega_1 2mT_s) & \cdots & \sin(\omega_1(2P-1)T_s) \\ \cos(\omega_1 2mT_s) & \cdots & \cos(\omega_1(2P-1)T_s) \\ \vdots & \cdots & \vdots \\ \sin(\omega_m 2mT_s) & \cdots & \sin(\omega_m(2P-1)T_s) \\ \cos(\omega_m 2mT_s) & \cdots & \cos(\omega_m(2P-1)T_s) \end{bmatrix} \\
\mathbf{f_1} &= \begin{bmatrix} \mathbf{r}_y(2P) \\ \vdots \\ \mathbf{r}_y(np+2P-1) \end{bmatrix}; \mathbf{f}_2 = \begin{bmatrix} \sin(\omega_\mathbf{1} 2PT_s) \\ \cos(\omega_\mathbf{1} 2PT_s) \\ \vdots \\ \sin(\omega_m 2PT_s) \\ \cos(\omega_m 2PT_s) \end{bmatrix}
\end{aligned}
\tag{35}
$$

References

[1] J. Munoa, X. Beudaert, Z. Dombovari, Y. Altintas, E. Budak, C. Brecher, G. Stepan, Chatter suppression techniques in metal cutting, CIRP Annals 65 (2) (2016) 785–808.

[2] I. E. Minis, E. B. Magrab, I. O. Pandelidis, Improved methods for the prediction of chatter in turning, Part 2: Determination of cutting process parameters, Journal of Manufacturing Science and Engineering, Transactions of the ASME 112 (1) (1990) 21–27. doi:10.1115/1.2899291.

[3] O. Özşahin, E. Budak, H. N. Özgüven, Investigating dynamics of machine tool spindles under operational conditions, Advanced Materials Research 223 (2011) 610–621. doi:10.4028/www.scientific.net/AMR.223.610.

[4] I. Zaghbani, V. Songmene, Estimation of machine-tool dynamic parameters during machining operation through operational modal analysis, International Journal of Machine Tools and Manufacture 49 (12-13) (2009) 947–957. doi:10.1016/j.ijmachtools.2009.06.010.

[5] M. Farhadmanesh, K. Ahmadi, Online identification of mechanistic milling force models, Mechanical Systems and Signal Processing 149 (2021) 107318.

[6] O. Özşahin, E. Budak, H. N. Özgüven, In-process tool point FRF identification under operational conditions using inverse stability solution, International Journal of Machine Tools and Manufacture 89 (2015) 64–73. doi:10.1016/j.ijmachtools.2014.09.014.

[7] N. Grossi, L. Sallese, A. Scippa, G. Campatelli, Improved experimental-analytical approach to compute speed-varying tool-tip FRF, Precision Engineering 48 (2017) 114–122. doi:10.1016/j.precisioneng.2016.11.011.

[8] M. Eynian, In-process identification of modal parameters using dimensionless relationships in milling chatter, International Journal of Machine Tools

and Manufacture 143 (December 2018) (2019) 49–62. doi:10.1016/j.ijmachtools.2019.04.003.

[9] Y. P. Liu, Y. Altintas, In-process identification of machine tool dynamics, CIRP Journal of Manufacturing Science and Technology 32 (2021) 322–337. doi:10.1016/j.cirpj.2021.01.007.

[10] M. Postel, B. Bugdayci, F. Kuster, K. Wegener, Neural network supported inverse parameter identification for stability predictions in milling, CIRP Journal of Manufacturing Science and Technology 29 (2020) 71–87. doi:10.1016/j.cirpj.2020.02.004.

[11] J. Karandikar, A. Honeycutt, T. Schmitz, S. Smith, Stability boundary and optimal operating parameter identification in milling using Bayesian learning, Journal of Manufacturing Processes 56 (March) (2020) 1252–1262. doi:10.1016/j.jmapro.2020.04.019.

[12] M. Löser, A. Otto, S. Ihlenfeldt, G. Radons, Chatter prediction for uncertain parameters, Advances in Manufacturing 6 (3) (2018) 319–333.

[13] E. Graham, M. Mehrpouya, S. Park, Robust prediction of chatter stability in milling based on the analytical chatter stability, Journal of Manufacturing Processes 15 (4) (2013) 508–517.

[14] K. Li, S. He, H. Liu, X. Mao, B. Li, B. Luo, Bayesian uncertainty quantification and propagation for prediction of milling stability lobe, Mechanical Systems and Signal Processing 138 (2020) 106532. doi:10.1016/j.ymssp.2019.106532.

[15] G. Chen, Y. Li, X. Liu, B. Yang, Physics-informed Bayesian inference for milling stability analysis, International Journal of Machine Tools and Manufacture 167 (February) (2021) 103767. doi:10.1016/j.ijmachtools.2021.103767.

[16] S. Kim, K. Ahmadi, Estimation of vibration stability in turning using operational modal analysis, Mechanical Systems and Signal Processing 130 (2019) 315–332.

[17] Y. Ding, L. Zhu, X. Zhang, H. Ding, A full-discretization method for prediction of milling stability, International Journal of Machine Tools and Manufacture 50 (5) (2010) 502–509.

[18] R. Plaut, K. Huseyin, Derivatives of eigenvalues and eigenvectors in non-self-adjoint systems., AIAA journal 11 (2) (1973) 250–251.

[19] A. Nobari, H. Ouyang, P. Bannister, Statistics of complex eigenvalues in friction-induced vibration, Journal of Sound and Vibration 338 (2015) 169–183.

[20] P. Mohanty, D. J. Rixen, Operational modal analysis in the presence of harmonic excitation, Journal of sound and vibration 270 (1-2) (2004) 93–109.

[21] N. M. M. Maia, J. M. M. e Silva, Theoretical and experimental modal analysis, Research Studies Press, 1997.

[22] J. S. Bendat, A. G. Piersol, Engineering applications of correlation and spectral analysis, New York (1980).

[23] J. L. Beck, L. S. Katafygiotis, Updating models and their uncertainties. i: Bayesian statistical framework, Journal of Engineering Mechanics 124 (4) (1998) 455–461.

[24] S. H. Cheung, S. Bansal, A new gibbs sampling based algorithm for bayesian model updating with incomplete complex modal data, Mechanical Systems and Signal Processing 92 (2017) 156–172.

[25] J. L. Beck, Bayesian system identification based on probability logic, Structural Control and Health Monitoring 17 (7) (2010) 825–847.

[26] J. L. Beck, K.-V. Yuen, Model selection using response measurements: Bayesian probabilistic approach, Journal of Engineering Mechanics 130 (2) (2004) 192–203.

[27] B. Goller, J. Beck, G. Schueller, Evidence-based identification of weighting factors in bayesian model updating using modal data, Journal of Engineering Mechanics 138 (5) (2012) 430–440.

[28] W. Betz, I. Papaioannou, D. Straub, Transitional markov chain monte carlo: observations and improvements, Journal of Engineering Mechanics 142 (5) (2016) 04016016.

[29] Y. Altintas, A. Ber, Manufacturing automation: metal cutting mechanics, machine tool vibrations, and cnc design, Appl. Mech. Rev. 54 (5) (2001) B84–B84.

[30] Y. Altintaş, E. Budak, Analytical prediction of stability lobes in milling, CIRP annals 44 (1) (1995) 357–362.